Journal of Sound and Vibration 447 (2019) 61–77

Contents lists available at ScienceDirect

Journal of Sound and Vibration

journal homepage: www.elsevier.com/locate/jsvi

Dynamic disturbance force measurement platform for large moving device in spacecraft

Mingyi Xia [a, b], Zhenbang Xu [a, *], Kang Han [a, b], Qi Huo [a], Ang Li [a, b]

[a] Innovation Lab of Space Robot System, Space Robotics Engineering Center, Changchun, Institute of Optics, Fine Mechanics and Physics, Chinese Academy of Sciences, Changchun, 130033, China
[b] University of Chinese Academy of Sciences, Beijing, 100049, China

ARTICLE INFO

Article history:
Received 20 July 2018
Received in revised form 23 November 2018
Accepted 27 January 2019
Available online 30 January 2019
Handling Editor: H.Ouyang

Keywords:
Space telescope
Generalized force
Micro-vibration
Redundant layout
Finite element analysis
Dynamic calibration

ABSTRACT

Analysis and suppression of micro-vibration is an important concern in the research related to large space telescopes. In accordance with this concern, a series of works, including simulations and experiments, must be carried out to assess these micro-vibrations. Accurate disturbance data from the vibration source of a large space telescope serves as the basis for the required micro-vibration research; therefore, this paper describes the development of a novel generalized disturbance force measurement platform for large device vibration sources. Use of redundant piezoelectric sensors allows the structural stiffness and the measurement precision of the platform to be improved. The design of the mechanism, the simulation analysis and the calibration algorithms of the developed platform are analyzed theoretically. Based on the results of this analysis, a prototype system is designed and tested. The experimental results show that the dynamic relative error within the 8–800 Hz range is largely less than 5%, while the static relative error is less than 5%. The linearity of the generalized forces within a 40 kN range is within 0.1%FS, while the repeatability is within 0.1%FS.

1. Introduction

Micro-vibration is a difficult but inevitable problem that must be resolved for highly stable spacecraft such as large space telescopes [1–5]. Moving devices, such as a control moment gyroscope (CMG), a momentum wheel, a cryocooler, or a relay antenna, can often cause the resonance of dense modes to affect the telescope's line of sight (LOS). With the increasingly large scale of spacecraft, the masses and volumes of these active devices are also increasing, which means that the resulting micro-vibrations are becoming increasingly serious. Therefore, analysis and suppression of these micro-vibrations will be necessary. Based on experience gained from the Hubble Space Telescope (HST) and the James Webb Space Telescope (JWST) [6–10], accurate disturbance data from vibration sources can serve as a basis for micro-vibration research. The weight of China's space telescope is likely to be more than fifteen tons and its primary mirror has a diameter of 2 m. The telescope's optical resolution will be comparable to that of the HST, and its field of view will be more than 300 times that of the HST. If it is in orbit for 10 years, this telescope will be able to observe more than 40% of the area of the sky, equivalent to approximately 17500 square

* Corresponding author.
E-mail address: xuzhenbang@gmail.com (Z. Xu).

https://doi.org/10.1016/j.jsv.2019.01.053

degrees. This telescope is still at the design stage. However, because of its greater mass and higher precision requirements, micro-vibration measurements of the vibration sources will be more difficult.

In recent years, research into micro-vibration measurements was mainly aimed at small vibration sources that were used in satellites [11]. However, the masses of the moving devices are tending to become larger to provide the required output forces and moments. For example, the maximum output of a CMG is 500 Nm, while its mass is 90 kg, and six CMGs are usually used in a group for large space telescopes. Fig. 1 shows a common CMG disturbance waterfall curve. According to the micro-vibration disturbance mechanism, the disturbances can be divided into two main categories. 1) Active disturbances. This category mainly includes the harmonic disturbances generated by rotation of the rotor, dynamic imbalance, rolling bearing defects and motor disturbances. 2) Structural natural frequency responses. These responses are caused by the resonance of the active disturbance and the internal structure, including the structural modal curves that do not change with the rotation speed and V-shaped curves. In addition, a significant amplification occurs when the two types of curve intersect. According to the method of micro-vibration spectrum analysis, the sources disturbance can be divided into three categories: 1) stationary random disturbances; 2) harmonic disturbances; and 3) nonstationary disturbances. The frequency distributions of stationary random disturbances and harmonic disturbances are wide, generally ranging up to tens of thousands of hertz, while their amplitudes can range from a few millinewtons to hundreds of newtons. If the stiffness of the measurement platform is insufficient, resonance between the vibration source and the platform during the measurement process is inevitable and results in decreasing measurement precision. In this case, it becomes difficult to measure this type of micro-vibration disturbance force data using traditional force measurement platforms. We therefore require a new force measurement platform that can meet the measurement requirements of large space telescopes in terms of its stiffness, precision and measurement range. We must also ensure that the fundamental frequency of the platform is more than 1000 Hz, that the force test resolution reaches 0.001 N when the signal-to-noise ratio (SNR) is greater than 10, that the dynamic measurement precision is within 5% in the 8–800 Hz range, and that the load capacity is at least 3 tons.

Sensors with carrying capacities of between 10 and 2000 kN are usually called heavy force sensors [12], and the maximal rated loads of the heavy force platforms used on such heavy load operating equipment can reach 100 MN or more. Based on the research on heavy force measurement technology, the force measurement platforms can mainly be classified into strain and piezoelectric types. The strain-type platforms can be designed to be compact, lightweight, and simple structures that are easy to use and offer a fast response. However, for the large strains caused by heavy loads, obvious nonlinear errors often occur within the output signals from these platforms. In addition, the parameters of these devices, such as the coefficients of resistance and sensitivity, are often sensitive to temperature variations. Therefore, these strain-type sensors [13–19] are now more commonly used in robot wrist sensors. Piezoelectric sensors, however, have a stronger ability to withstand heavy loads and offer higher stability (see e.g., the Kistler measurement platform), which means that the piezoelectric-type sensors will usually offer better performance than strain-type sensors for dynamic measurement of heavy loads.

The spatial disturbances that emanate from the vibration sources of large space telescopes are generally multi-dimensional. To test these types of disturbance forces, a specific configuration composed of multiple piezoelectric sensors is required. In previous research [20–22] on piezoelectric measurement platforms, the Stewart platform was most commonly used, but its loose and bulky structure will reduce the stiffness of the platform, and thus the coupling of the platform and the vibration source is inevitable. This limits the application of the Stewart platform in heavy load measurements. Other platforms have mostly used orthogonal layouts. This type of layout can take the effects of the stiffness and the measurement precision into account, and its design can be varied, as in Li's design [12] of a six-axial piezoelectric force sensor for measurement of extremely heavy loads. A study of the spatial layout of the force-sensing elements, the preliminary load sharing method, and the structural response of the sensor was performed. Soon after that study, Li [23] used adjustable load sharing devices to develop another parallel piezoelectric sensor for heavy loads, which was applied to the wrist joints of a robot. Liang [24] investigated the performance of piezoelectric lead zirconate titanate (PZT) thick-film pressure sensors and fabricated an unimorph sensor structure. Durand [25] invented a measurement sensor for a linking wrench, where the sensor consisted of six piezoelectric cylinders mounted and fastened in different directions between two plates. Sujan [26] designed a stainless steel resonant pressure sensor that used both piezoelectric excitation and detection. The sensor consisted of a sensing

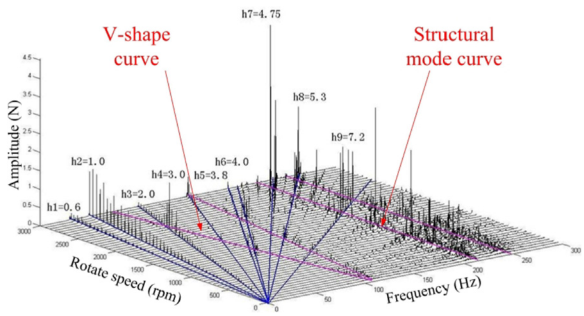

Fig. 1. Disturbance waterfall curve of CMG.

diaphragm, inclined trusses, vertical mounts and a resonating beam, and provided improved nonlinearity performance and maximum hysteresis.

The above piezoelectric measurement systems, which have structures and principles that are intended for different working environments and different test requirements, are used for reference for the design of the structure proposed in this paper, but they are more often used to measure the six-dimensional forces of small space structures for force feedback. Their stiffness and measurement ranges and working principles are not suitable for large vibration source measurements, about which there are almost no relevant publications in the literature. Based on this approach, a novel generalized force piezoelectric measurement platform is proposed that is applied to the micro-vibration measurement of large vibration sources. The platform uses eight piezoelectric sensors in a redundant layout. To improve the stiffness and the precision of the platform, systematic work was carried out in terms of the mechanism design, the related simulation analyses and the calibration algorithms. Section 2 describes the basic design of the proposed platform, and the effects of the sensor position on the stiffness are verified by finite element analysis (FEA). In Section 3, the working principle of the platform is analyzed theoretically to improve the test precision. Experiments are performed to verify the dynamic and static mechanical properties of the measurement platform in Section 4. The conclusions are then summarized in the final section.

2. Structural design and analysis

Different measurement platforms can mainly be distinguished by their variable sensor elements and their layout. However, all platforms can be described using the same basic model: a load platform, a base and the sensors that connect the load platform to the base.

Fig. 2 shows a schematic of the working principle of the platform. During measurements, the platform is fixed on a vibration isolation platform through its base, and the vibration source to be measured is mounted on the load platform. When the vibration source is operating, the disturbance force is transmitted to the piezoelectric sensors, which produce output signals that can be converted into the generalized disturbing force of the measured vibration source mounting interface using a calibration matrix.

2.1. Basic layout of the structure

In measurement of micro-vibrations, insufficient platform stiffness will cause structural resonance that leads to signal distortion, so it can be said that the stiffness determines the measurement precision. In addition, based on previous research [27], increasing the number of sensors used can effectively improve both the stiffness and the measurement precision of the platform. Therefore, it is essential that sufficient numbers of sensors are available for measurement of the micro-vibrations; a redundant layout for the sensors will thus form the basis of this design. In accordance with the stiffness and structural layout requirements, the number of sensors used in this work is set at eight.

Fig. 3 shows the basic structure of the platform. Eight sensors are installed in this measurement platform. Half of the sensors are distributed at the four corners of the base, which is connected to the load platform, to collect the vertical force and moment components; the other sensors are located with rotational symmetry about the four corners of the load platform to collect the torque and horizontal force components, as shown in Fig. 4. Compared to 4-point connection structure, this 8-point redundant form can effectively increase stiffness.

The sensing element of each sensor is made from lead zirconate titanate (PZT), which has a piezoelectric constant of 330 pC/N, and the measurement range of each element can reach a minimum of 10 kN, which means that the measurement range of the platform in this layout is more than 40 kN. The PZT is axially polarized and operated in a differential connection mode, while each sensor takes the form of a ring, with an outer ring diameter of 19 mm, an inner ring diameter of 7.5 mm, and ring thickness of 5 mm. The superposition of two sensing layers is then used to improve the measurement precision and resolution, as illustrated in Fig. 5.

To ensure platform precision, we tested the resolution and the linearity of the designed sensor. The sensor output as a time-domain signal is shown in Fig. 6; by inputting impact forces with different amplitudes, the sensitivity coefficient of the

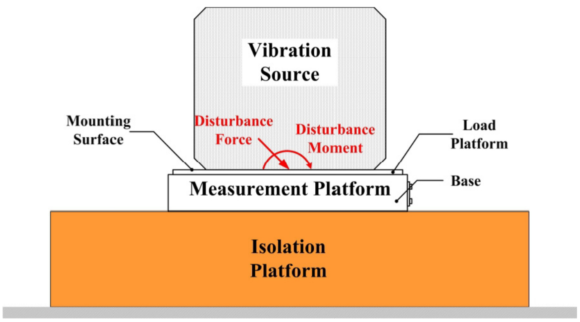

Fig. 2. Schematic showing the working principle of the measurement platform.

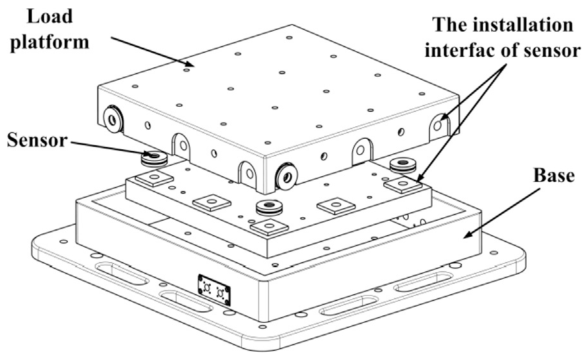

Fig. 3. Basic structure of the platform.

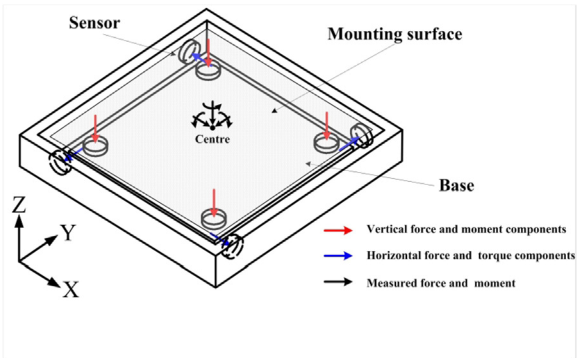

Fig. 4. Basic layout of the force sensors.

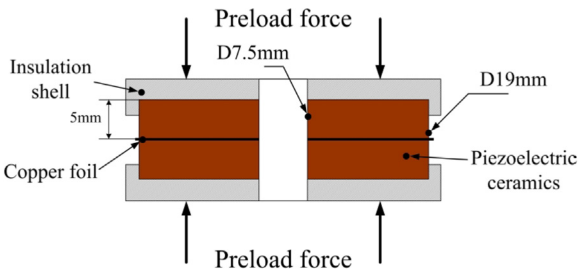

Fig. 5. Structural schematic of the force sensor.

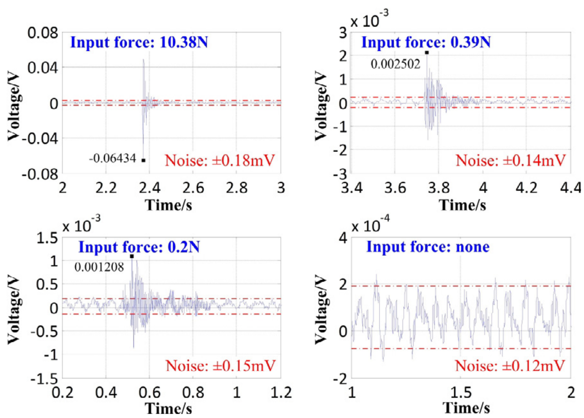

Fig. 6. Performance test curves of piezoelectric sensor.

sensor was experimentally determined to be approximately 6.2 mV/N axially. However, in the absence of an input force, the data acquisition device (precision: ±0.02 dB (0.2% FS) @ 1 kHz; SignalCalc ACE, Data Physics Corporation, San Jose, CA, USA) has a noise input of 0.12 mV. This means that the resolution of the platform is largely determined by the resolution of the sensor and the noise environment. The noise amplitude is constant under the same conditions, when the input force is 0.2 N (in the time domain), the SNR for acquisition in the time domain is just under 10, and the output waveform and amplitude are still consistent with the input impact forces. As the magnitude decreases, the SNR will also continue to decrease; therefore, in this case, the resolution of the platform is mainly determined by the layout of the sensors and the random environment, which is analyzed in Section 3.2 and tested in Section 4.2. Additionally, the sensor shows very good linearity based on an analysis of the test data. After ensuring the resolution and the linearity of the sensors, the specific positioning of the sensors will be defined in the next section to obtain improved platform stiffness.

2.2. Finite element analysis of the structure

To obtain the better platform performance we need to improve the platform structure through FEA. Based on the characteristics of the disturbance signal (micro-vibration, coupling) and the properties of the piezoelectric ceramic (high sensitivity, good linearity), the design focus of the FEA is turned towards the stiffness to ensure that the transfer function will be sufficiently stable within the test frequency range [30,31]. The sensors should be the only connection between the load platform and the base. The stiffness of the platform is largely determined by the positioning of the sensors; therefore, in this work, Nastran software has been used to analyze the stiffness of the platform. The objective of the design is to determine the natural frequency of the platform. After the structural response has been obtained, the sensitivity of the various design variables to the structural response can be determined. Based on this new design, we can then modify the model used in the analysis and begin write iteration until the reliability and design requirements of the platform are met [13]. The reliability requirements are mainly based on whether the boundary and loading conditions of the results are actually credible.

In this design, we still use a symmetrical distribution for the sensors to ensure that the natural frequency of the platform is maximized in all directions. While asymmetry will lead to different natural frequencies in the x, y direction, although it may result in better stiffness in one direction, it will cause difficulties in the structural design, manufacturing and the calibration algorithm. After comprehensive consideration of the possible distributions, we adopted a symmetrical form. Therefore, the sensor distribution can only be determined based on three parameters (X1, X2 and X3), which are shown in Fig. 7. Here, X1 and X2 determine the positions of the four vertical direction sensors (or Z-axis sensors), while X3 determines the positions of the horizontal direction sensors (or X&Y-axis sensors). Fig. 8 shows the structural finite element model. The main material used for the structure is ^{40}Cr, which has an elastic modulus of 206780 MPa, a Poisson ratio of 0.277, density of 7.82×10^3 kg/m^3, and a yield strength of 780 MPa. In addition, the elastic modulus of the piezoelectric ceramic (PZT) was set at 76500 MPa. These material parameters were obtained experimentally, and the finite element model follows the assembly relationship of the actual platform model. Hexahedral elements were mainly used, the chamfering was simplified, and small parts were ignored, with their masses being attached to that of the main structure; connection of the components was achieved through node coupling, and the piezoelectric ceramic sensors are connected while neglecting preloading, such that only the stiffness is provided. The number of elements in the model is 88146, the number of nodes is 119166, and the number of multi-point

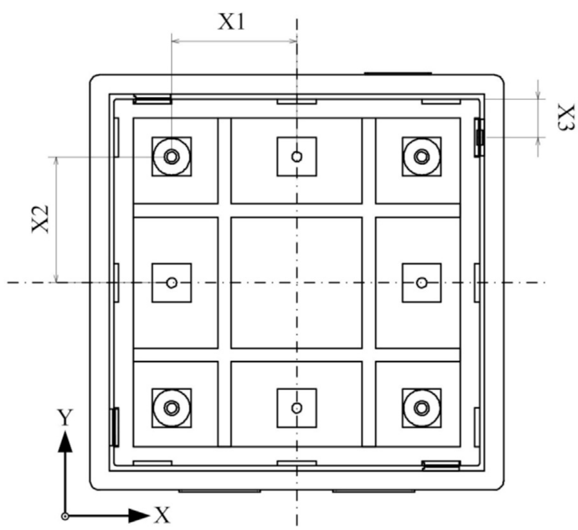

Fig. 7. Distribution position parameters of the sensors.

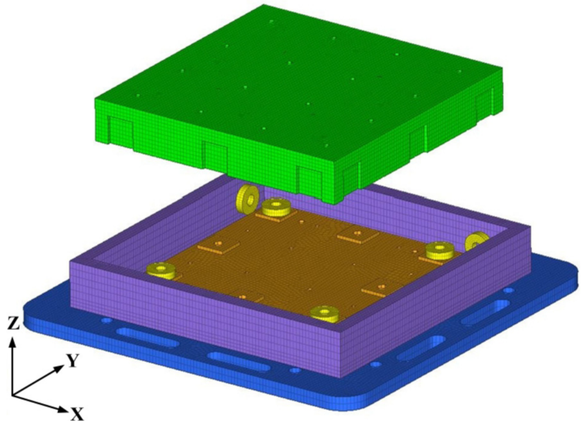

Fig. 8. Finite element model of the measurement platform.

constraints (MPC) is 0. The first four modes of the model provided by FEA are shown in Fig. 9. The first-order mode of the platform is the diagonal angle twists of the load platform, while the second- and third-order modes are the adjacent angle twists of the load platform, and the fourth-order mode represents a twist of the base. To obtain a better platform stiffness value, the effects of X1, X2, and X3 on each of the order modes are considered via the FEA.

Assuming that the value of X3 is constant, the effects of sensor positions X1 and X2 on the stiffness are as shown in Fig. 10. From the cloud images, we know that peaks are evident for the natural frequencies of the first four orders as X1 and X2 change, and their trends are almost identical in that the natural frequencies reach their maxima at the same position. Therefore, when only the stiffness is considered, the optimal values of X1 and X2 can be determined, and are both 85 mm here.

Because the position of the horizontal sensor is determined based on X3 alone, however, the trends of the natural frequencies of the first four orders are not similar; when only the peak of the frequency is considered, there is no optimal value for X3. Therefore, the work in this paper uses the bandwidth as another measure for evaluation of the stiffness, because the bandwidth of the platform must be as narrow as possible to make it easier to avoid structural resonance. In this case, the analysis results could be determined based on the weighted average of the peaks of the natural frequencies of the first four orders, and their bandwidths are given by Eq. (1). Here, W_{14} represents the bandwidth at the natural frequencies of the first four orders, $Freq_i$ is the i-th order frequency, $n_1 = 0.25$, $n_2 = 0.6$, $n_3 = 0.05$, $n_4 = 0.05$, and $n_5 = 0.05$. The final value of X3 is 56 mm, as shown in Fig. 11.

$$X_{ob3} = \frac{n_1 \bullet W_{14} + \sum_{i=1}^{4} n_{i+1} \bullet Freq_i}{\sum_{i=1}^{5} n_i} \tag{1}$$

Following the above analysis process, the specific sensor position values that were obtained are listed in Table 1. From the results of the FEA, the first order mode of the platform is at 1343 Hz, which does meet the original design requirement. However, when moving devices with large masses are measured, the coupling effect will cause the test system's own stiffness distribution to change. Using rigid-flexible coupling theory, we can obtain a more accurate sensor position for prediction of the stiffness distribution, which may allow the precision of the calibration matrix to be further improved; this part of the work will be completed as part of our future work.

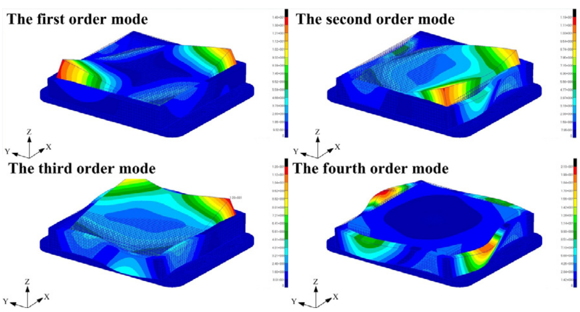

Fig. 9. Cloud chart showing the first four order modes of the platform.

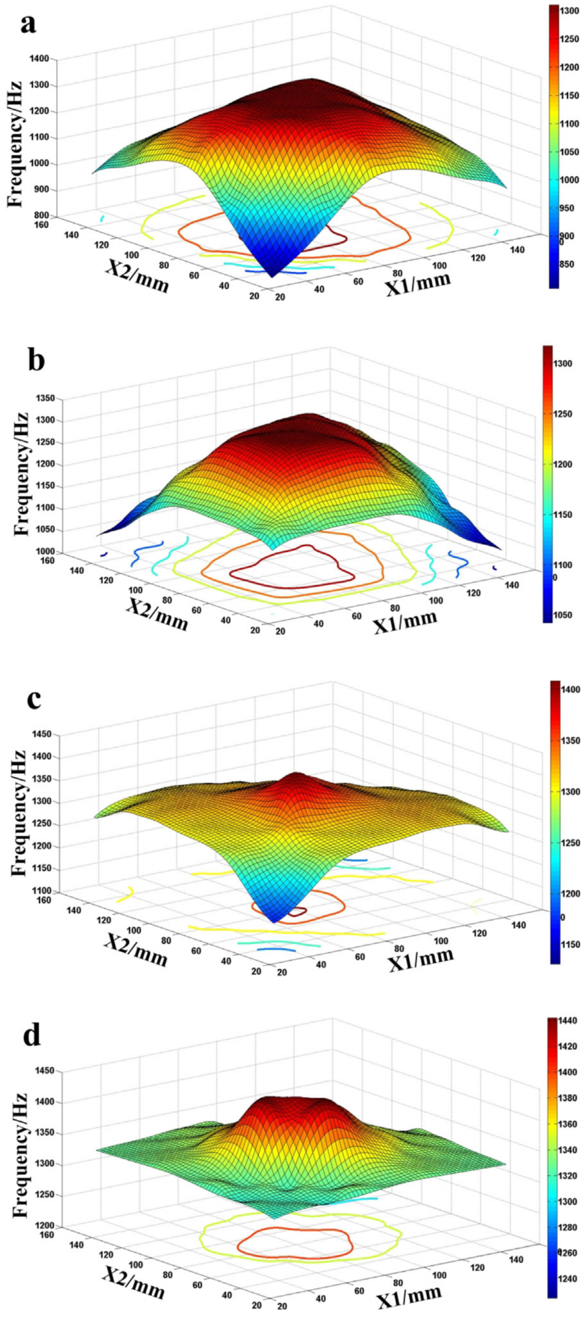

Fig. 10. Gradient charts of the first four order modes with X1 and X2: (a) The first order natural frequency; (b) The second order natural frequency; (c) The third order natural frequency; (d) The fourth order natural frequency.

3. Working principle

3.1. Redundant calibration theory

The forces that are associated with micro-vibrations can vary from a few Newtons to hundreds of Newtons. With the dense modes that are available from the large space telescope data, the spectral information can be analyzed more easily. Therefore, during the micro-vibration measurements, the platform calibration should be completed using frequency domain analysis. As shown in Fig. 12, for the proposed measurement platform, point O' represents the center of the vibration source that outputs the actual six-dimensional disturbance force. The equivalent center is the geometrical center of the mounting surface of the

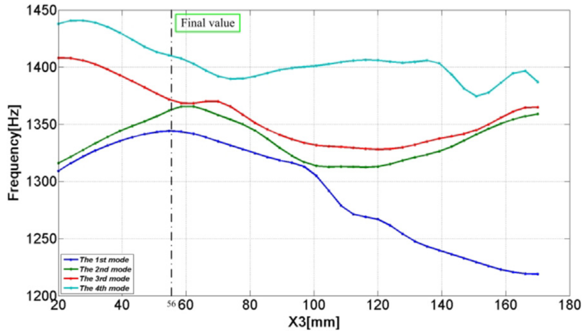

Fig. 11. Curves of the natural frequencies of the first four orders with X3.

Table 1
Final sensor position values obtained from the FEA of the platform.

Optimal value (mm)	First four natural frequency (Hz)			
X1 = 85; X2 = 85; X3 = 56	$f_1 = 1343.4$	$f_2 = 1356.5$	$f_3 = 1378.4$	$f_4 = 1414.4$

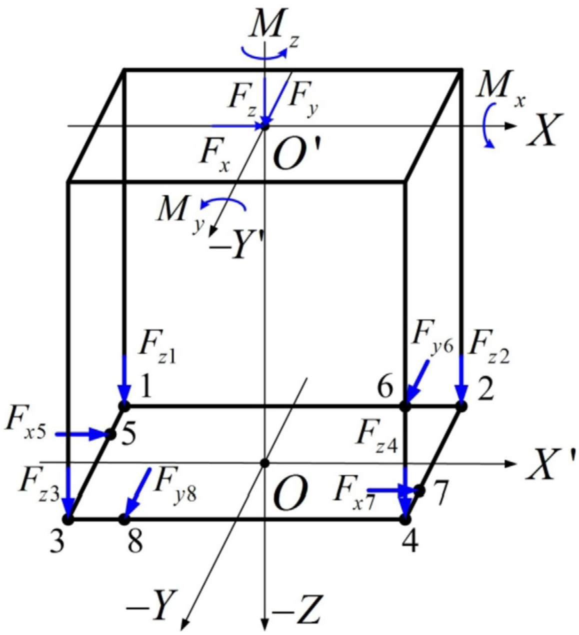

Fig. 12. Specific layout of force sensing elements.

load platform, which is denoted by point *O*. During testing, and using the basic layout of the eight force sensors, the platform can obtain the disturbance distribution that corresponds to point *O'*, and this distribution can then be converted into the six-dimensional disturbance force that corresponds to point *O* using the dynamic calibration matrix.

In platform calibration, the basic assumption that is made for the nonrigid body when modeling the sensor system is that the platform's response is linear; i.e.,

$$\mathbf{V}(\omega) = \mathbf{H}(\omega)\mathbf{F}(\omega) \tag{2}$$

where $\mathbf{V}(\omega)$ is the output spectrum vector matrix from eight sensors, $\mathbf{F}(\omega)$ is the output spectrum vector matrix from the measured vibration source, and $\mathbf{H}(\omega)$ is the frequency response function matrix. The disturbing force has a six-dimensional output, so if the number of sensors contained in Eq. (2) is more than six, we can call this process redundant observation. The frequency response function matrix $\mathbf{H}(\omega)$ will no longer be a square matrix, and the generalized inverse of $\mathbf{H}(\omega)$ must then be calculated to obtain the measured output spectrum; i.e.,

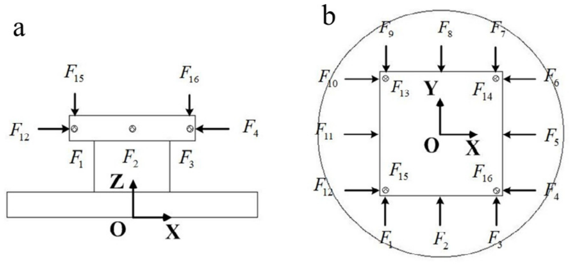

Fig. 13. Layout of the load points for the calibration process: (a) front view, and (b) top view.

$$\mathbf{F}(\omega) = \left[\mathbf{H}^{\mathrm{H}}(\omega)\mathbf{H}\right](\omega)^{-1}\mathbf{H}^{\mathrm{H}}(\omega)\mathbf{V}(\omega) \tag{3}$$

Usually, the dynamic response $\mathbf{V}(\omega)$ is relatively easy to obtain, while determination of the frequency response function matrix $\mathbf{H}(\omega)$ is difficult, which is a reflection of the relationship between the different discrete excitation points and response points. Therefore, to determine each matrix element, rigid calibration equipment is mounted on the upper surface of the load platform, as shown in Fig. 13; the fundamental frequency of this calibration equipment is more than three times the maximal detection frequency, which means that it is considered to be a rigid body relative to the platform. All the calibration excitation forces are thus equivalent to six generalized forces acting at the center O of the mounting surface.

First, the calibration forces are converted into equivalent forces that act on the center O of the mounting surface, i.e.,

$$\mathbf{F}_{6\times n}(\omega) = \mathbf{C}_{6\times n}\,\mathbf{F}'_{n\times n}(\omega) \tag{4}$$

In Eq. (4), n indicates the number of calibration forces used in the test. In this work, n is 16, as shown in Fig. 11. In addition, $\mathbf{F}$ represents the excitation force that is equivalent to O, $\mathbf{F}'$ represents the actual loaded force, which is a diagonal matrix, and $\mathbf{C}$ represents the transition matrix.

The relationship between the equivalent load and the output signal of the force sensor is:

$$\mathbf{W}_{6\times 8}(\omega)\mathbf{V}_{8\times n}(\omega) = \mathbf{F}_{6\times n}(\omega) \tag{5}$$

where $\mathbf{W}$ is the inverse of the frequency response function matrix (i.e., the calibration matrix) and $\mathbf{V}$ represents the response signals of the eight force sensors. From Eq. (5), we see that when $\mathbf{V}$ has a generalized inverse, $\mathbf{W}$ can be expressed as follows:

$$\mathbf{W}_{6\times 8}(\omega) = \mathbf{F}_{6\times n}(\omega)\mathbf{V}^{\mathrm{H}}(\omega)\left[\mathbf{V}(\omega)\mathbf{V}^{\mathrm{H}}(\omega)\right]^{-1} \tag{6}$$

Substitution of Eq. (4) into Eq. (6) then gives:

$$\mathbf{W}_{6\times 8}(\omega) = \mathbf{C}_{6\times n}\mathbf{F}'_{n\times n}(\omega)\mathbf{V}^{\mathrm{H}}(\omega)\left[\mathbf{V}(\omega)\mathbf{V}^{\mathrm{H}}(\omega)\right]^{-1} \tag{7}$$

In the micro-vibration measurements with eight sensor output signals and $\mathbf{W}(\omega)$, the measured equivalent force $\mathbf{F}_o(\omega)$ at point O is given by

$$\mathbf{F}_o(\omega) = \mathbf{W}(\omega)\mathbf{V}(\omega) \tag{8}$$

3.2. Measurement precision analysis

The potential measurement errors include both force sensor errors and calibration errors. For the force sensor errors, system errors can be corrected by selecting more accurate data acquisition devices and calibration algorithms, while random sensor errors can be improved by increasing the number of sensors used. The calibration errors mainly stem from random errors in the calibration force and system errors during the calibration process. With regard to the system errors during the calibration process, we performed the following analysis.

To determine the effects of the redundancy on the measurement precision of the platform, the calibration process errors are analyzed theoretically. Similar to Eq. (2), the calibration process can be defined as follows:

$$\mathbf{V} = \mathbf{T} \cdot \mathbf{H} \tag{9}$$

where **V** is the output of the sensor, **T** is the generalized calibration force that acts on the calibration tooling (see Fig. 11), and H is a generalized matrix that is determined based on the platform structure. The essence of the calibration procedure is the way in which the matrix **H** is obtained using **T** and the sensor output **V**. In this paper, based on the redundant layout used for the sensors, the theoretical precision of the redundant observation can be deduced using norm theory. First, the calibration force is $\mathbf{T}_{ik}$ (where $i = 1, 2 \ldots n$, and $k = 1, 2 \ldots 6$), where i indicates the number of calibration forces, k represents the indexes of the six components of the calibration generalized force, and $\mathbf{V}_{ij}$ ($j = 1, 2 \ldots m$) is the output of every sensor when j is the number of sensors. From Eq. (10) the linear equations for the j-line elements of matrix **A** can be obtained.

$$\begin{array}{l} \mathbf{V}_{1j} = \mathbf{T}_{11}\mathbf{H}_{1j} + \mathbf{T}_{12}\mathbf{H}_{2j} + \cdots + \mathbf{T}_{16}\mathbf{H}_{6j} \\ \mathbf{V}_{2j} = \mathbf{T}_{21}\mathbf{H}_{1j} + \mathbf{T}_{22}\mathbf{H}_{2j} + \cdots + \mathbf{T}_{26}\mathbf{H}_{6j} \\ \qquad \vdots \\ \mathbf{V}_{nj} = \mathbf{T}_{n1}\mathbf{H}_{1j} + \mathbf{T}_{n2}\mathbf{H}_{2j} + \cdots + \mathbf{T}_{n6}\mathbf{H}_{6j} \end{array} \tag{10}$$

This means that

$$\mathbf{V}_{n\times m} = \mathbf{T}_{n\times 6} \cdot \mathbf{H}_{6\times m} \tag{11}$$

When the number of calibration forces $n > 6$, Eq. (11) has no unique solution and only has an approximate solution. The generalized inverse matrix for **F** is known, and thus

$$\mathbf{H}_{6\times m} = \left(\mathbf{F}^{\mathrm{T}}\mathbf{F}\right)^{-1}\mathbf{F}^{\mathrm{T}}\mathbf{V}_{6\times m} \tag{12}$$

This equation is known to have a least-squares solution, as given in Eq. (11). The solution for the error propagation can be expressed as:

$$\varepsilon_a = (\varepsilon_{FV} + \varepsilon_{FF})K\left(\mathbf{F}^{\mathrm{T}}\mathbf{F}\right) \tag{13}$$

where $K(\mathbf{F})$ is the error propagation factor, which has an upper bound. In addition, $\varepsilon_{FV} = \|\delta(\mathbf{F}^{\mathrm{T}}\mathbf{V})\| / \|\mathbf{F}^{\mathrm{T}}\mathbf{V}\|$, and $\varepsilon_{FF} = \|\delta(\mathbf{F}^{\mathrm{T}}\mathbf{F})\| / \|\mathbf{F}^{\mathrm{T}}\mathbf{F}\|$. This means that:

$$\varepsilon_{FF} = \frac{\left\|\left(\mathbf{F}^{\mathrm{T}} + \delta\mathbf{F}^{\mathrm{T}}\right)(\mathbf{F} + \delta\mathbf{F}) - \mathbf{F}^{\mathrm{T}}\mathbf{F}\right\|}{\|\mathbf{F}^{\mathrm{T}}\mathbf{F}\|} \le 2\varepsilon_F \tag{14}$$

$$\varepsilon_{FV} = \frac{\left\|\left(\mathbf{F}^{\mathrm{T}} + \delta\mathbf{F}^{\mathrm{T}}\right)(\mathbf{V} + \delta\mathbf{V}) - \mathbf{F}^{\mathrm{T}}\mathbf{V}\right\|}{\|\mathbf{F}^{\mathrm{T}}\mathbf{V}\|} \le \frac{\|\mathbf{F}^{\mathrm{T}}\|\|\mathbf{V}\|}{\|\mathbf{F}^{\mathrm{T}}\mathbf{V}\|}(\varepsilon_V + \varepsilon_F) \tag{15}$$

To determine the upper bound of Eq. (15), the norms of the vector and the matrix are assumed to be the 2-norms of the vector and the matrix, respectively. Depending on the nature of the vector 2-norm, we then obtain

$$\frac{\|\mathbf{F}^{\mathrm{T}}\mathbf{V}\|^2}{\|\mathbf{V}\|^2} = \frac{\mathbf{V}^{\mathrm{T}}\left(\mathbf{F}\mathbf{F}^{\mathrm{T}}\right)\mathbf{V}}{\mathbf{V}^{\mathrm{T}}\mathbf{V}} = R_{FF^T}(\mathbf{V}) > \delta_{\min}^2 = \left(\frac{1}{\left\|\left(\mathbf{F}^{\mathrm{T}}\right)^+\right\|}\right)^2 \tag{16}$$

where $R_{FF^T}(\mathbf{V})$ is the Rayleigh form of the matrix $\mathbf{F}\mathbf{F}^{\mathrm{T}}$, $\delta_{\min}$ is the least-positive odd value of the matrix $\mathbf{F}\mathbf{F}^{\mathrm{T}}$, and $(\mathbf{F}^{\mathrm{T}})^+$ is the pseudo-inverse matrix of the matrix $\mathbf{F}^{\mathrm{T}}$.

The number of conditions for a rectangular matrix is defined as:

$$\mathrm{cond}\left(\mathbf{F}^{\mathrm{T}}\right) \equiv \|\mathbf{F}\|\left\|\mathbf{F}^+\right\| = \mathrm{cond}(\mathbf{F}) \tag{17}$$

Then, Eq. (15) is transformed into

$$\varepsilon_{FV} \le \mathrm{cond}(\mathbf{F})(\varepsilon_V + \varepsilon_F) \tag{18}$$

Based on Eqs. (14) and (18), the error propagation given in Eq. (13) can be expressed as:

$$\varepsilon_a \leq \{[2 + \text{cond}(\mathbf{F})]\varepsilon_F + \text{cond}(\mathbf{F})\varepsilon_V\}K\left(\mathbf{F}^{\mathrm{T}}\mathbf{F}\right) \tag{19}$$

where $K(\mathbf{F}^{\mathrm{T}}\mathbf{F}) \approx [\text{cond}(\mathbf{F})]^2$. If $\mathbf{F}$ is the sub-orthogonal matrix, then

$$\mathbf{F}^{\mathrm{T}}\mathbf{F} = 1 \tag{20}$$

The matrix $\mathbf{F}$ has a minimum number of conditions (equal to 1). Based on Eq. (19), when ε_V and ε_F remain unchanged, the sensor has a minimum propagation error, i.e., the platform obtains its highest sensor calibration precision. The minimum propagation error is given by:

$$\varepsilon_a = 3\varepsilon_F + \varepsilon_V \tag{21}$$

Therefore, when the number of calibrated forces satisfies $n > 6$ in theory, the relative error that is associated with the calibration force matrix $\mathbf{F}$ is amplified when compared with $n = 6$. This indicates that the redundant calibration will cause magnification of the system error [34]. However, in actual dynamic measurements, the system error can be corrected by processing the acquired data, and because of the uncertainty of the calibration force caused by the unpredictable effects of the environment and personnel operations, the environmental random error of the calibrated force has a greater overall influence on the measurement results. When compared with system errors, the magnitude and the inter-dimensional interference of random errors are more obvious.

Based on error theory, random errors can only be reduced effectively by increasing the number of calibration forces and measurements. This indicates that a calibration strategy with more than six calibration forces should be adopted in this paper, where the number was set at 16 in this case [27–29]. Actual test results indicated that the test precision tends to improve as a result of this approach.

With regard to the errors from the sensors, as mentioned earlier, system errors can be corrected by selection of more accurate data acquisition devices and calibration algorithms. To reduce the interference from random errors and improve the platform resolution (SNR$\geqslant$10), to establish the minimum measurement error, the number of sensors used m should also be appropriate and should be greater than 6; m is thus set at 8 in this paper.

4. Experimental

Based on the FEA of the structure, we designed and manufactured a prototype measurement platform. To verify the simulation results and determine both the calibration matrix and the performance of the prototype, we set up two main experimental systems, in which the dynamic test system is mainly designed for dynamic calibration and dynamic mechanical performance testing of the proposed platform. The static test system is used to obtain the static mechanical properties of the platform, which include linearity, repeatability, and the static relative error [32,33].

4.1. Dynamic calibration test

Fig. 14 shows the dynamic calibration test system, the system includes calibration equipment, a data acquisition device (precision: ±0.1 dB; 652u-24 bit, IOtech, Norton, MA, USA), and an impact hammer (086C03, PCB; sensitivity: 2.25 mV/N; resolution: 0.02 N-rms; range: ±2200 N-pk.).

The natural frequency of the platform can be measured first. The hammer is used to input the required impact signal. The transfer function of the measurement platform, which was fixed to the isolation platform, was then obtained using the data acquisition device. Fig. 15 shows the transfer function curve of the platform that was obtained from the test. The natural frequency of the first order mode is 1340 Hz at a sampling frequency of 5120 Hz for the transfer function test, while the simulated result was 1343.4 Hz. This shows that the results of the FEA agree well with those obtained experimentally because of the precision of the modeling, and the goodness of fit proves that the simulation model can obtain the platform's dynamic performance with high precision. On the other hand, Fig. 15 could also show that there are some companion peaks near the fundamental frequency. This phenomenon is inevitable due to structural imperfection. So the stiffness needs to be kept high enough to avoid structural resonance, and for the test requirement in a range of 8–800 Hz, the fundamental frequency of 1340 Hz is enough.

The dynamic calibration matrix of the platform can also be obtained using this system. During the dynamic calibration experiment, an impact force was applied to the 16 calibration points in sequence using the hammer. Each point was loaded three times, and we then used the average values of the hammer and sensor output signals as the measured data to reduce the effects of random errors. From Eq. (7), we can obtain the calibration matrix $\mathbf{W}(\omega)$, as shown in Eq. (22). The frequency domain response curve of the platform and the transfer function curve can both be produced using a data sampling frequency of 2560 Hz, and a sampling time of 12.8 s. The length of each element $\mathbf{W}_{ij}(\omega)$ of the calibration matrix is 32768, which has an effective bandwidth of 1/12.8–1000 Hz (the effective coefficient of $\mathbf{W}(\omega)$ is 2.56.).

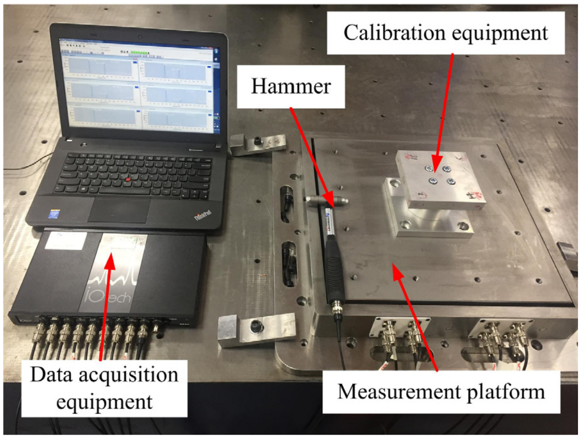

Fig. 14. Dynamic mechanical performance test system.

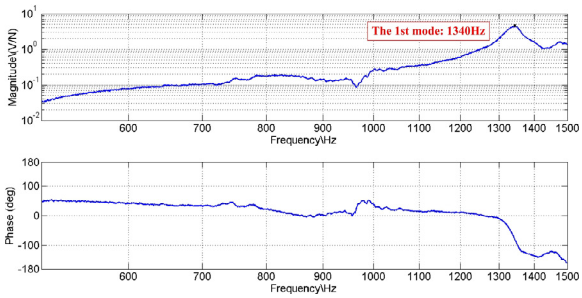

Fig. 15. Transfer function curve of the platform.

$$\mathbf{W}_{6\times 8}(\omega) = \begin{bmatrix} \mathbf{W}_{11}(\omega) & \cdots & \mathbf{W}_{18}(\omega) \\ \vdots & \ddots & \vdots \\ \mathbf{W}_{61}(\omega) & \cdots & \mathbf{W}_{68}(\omega) \end{bmatrix} \tag{22}$$

4.2. *Dynamic mechanical performance test*

After the dynamic calibration matrix $\mathbf{W}(\omega)$ was obtained, we set up a series of tests to determine the dynamic performance of the platform. First, we know that the calibration aims to acquire the energy distribution in the frequency domain. However, the amplitude of the disturbance ranges from a few millinewtons to hundreds of newtons for a large space telescope, and thus good dynamic linearity is the basis of stable measurement. For this reason, we detect the dynamic linearity of the platform based on a dynamic calibration system. Using a hammer, impacts with different amplitudes are input into the calibration equipment to obtain the transfer function between the calibration point and the sensor output, as shown in Fig. 16; this function can then be used to characterize the dynamic linearity of the sensor in both the axial direction and the shear direction.

Fig. 16 gives transfer functions for selected input impact amplitudes of 2.42 N, 25.33 N, and 112.24 N. Because the transfer function has been kept as flat as possible within the working frequency band (8–800 Hz), the transfer function curve fits most of the frequency bands well. However, it is not a flat curve near the platform resonance peak, which is unavoidable, so there are still deviations from the curve in the areas where the fluctuations are obvious. The measurement results can be accurately corrected via a calibration process. The test data statistics are presented in Table 2, and we consider the input of 25.33 N to be the reference. Table 2 lists the relative errors for impact inputs of 112.24 N and 2.24 N.

Table 2 shows that the maximum relative error is 8.4%, which occurs in the shear direction of the sensor, but also considers the randomness of the impact energy distribution in the various modes. This method is intended to characterize the sensor linearity over a wide frequency band. The method does not fully reflect the dynamic linearity of the six-dimensional output of the platform after dynamic calibration. Therefore, the dynamic linearity of the platform is detected using the sinusoidal signal response method. Fig. 17 shows a schematic diagram and a photograph of the dynamic linearity test system.

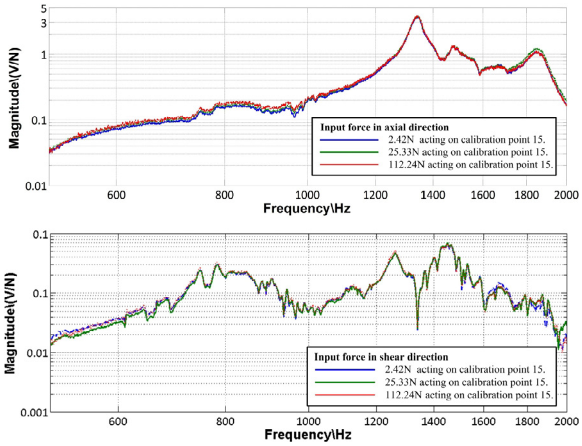

Fig. 16. Transfer function curves for different input impacts.

Table 2
Statistics of transfer function test results.

Frequency range		Input in axial direction (%)		Input in shear direction (%)	
		112.24 N	2.24 N	112.24 N	2.24 N
Low frequency	0–50	5.29%	5.70%	1.47%	4.26%
	50–100	5.33%	5.13%	1.51%	5.95%
Middle frequency	500–600	3.64%	4.31%	8.40%	8.15%
	600–700	5.36%	4.39%	5.32%	5.13%
	700–800	5.29%	5.70%	1.47%	3.26%
High Frequency	1200–1300	0.64%	4.31%	5.32%	6.13%
	1300–1400	1.62%	3.08%	2.92%	0.86%

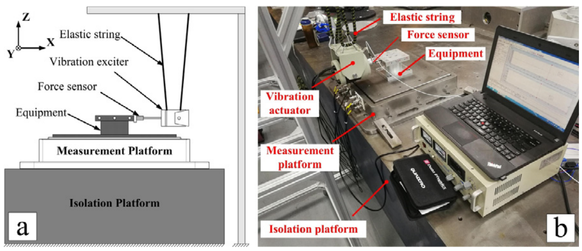

Fig. 17. Dynamic linearity test system. (a) Schematic illustration of the test system, and (b) photograph of the test system.

Using this system, we can obtain the dynamic linearity curve of the six-dimensional output at frequencies of 0.5 Hz, 30 Hz, 600 Hz, and 1200 Hz, as shown in Fig. 18. The input forces with their different amplitudes act on the equipment through the actuator, where the maximum is close to 100 N, and the minimum is approximately 1.4 N. Using the calibration matrix $\mathbf{W}(\omega)$, we can calculate the force and the moment of the platform output. The linearity error is fitted using the least squares method, and the relative error is within 3% at each point. With the platform measurement range acting as the reference, the dynamic linearity of the force and the moment of the platform are within 0.1%FS.

Next, we calculate the platform resolution using the obtained calibration matrix $\mathbf{W}(\omega)$. Based on the previous experiment, the sensor resolution has proved to be acceptable. The resolution of the platform is mainly determined by the precision of the environment acquisition. In addition, the data acquisition device used in the test has a range of 10 V and the effective number of bits (ENOB) for analog-to-digital conversion (ADC) is 24. The acquisition resolution of the device can theoretically reach $10/2^{24} = 5.96 \times 10^{-7}$ (V), which can then be converted into the resolution of the generalized disturbance force using the calibration matrix $\mathbf{W}(\omega)$. In addition, the platform resolutions of the six components are finally averaged in each frequency band. As shown in Table 3, the resolution statistics within the 8–200 Hz range are listed. The results show that with changes in frequency, the platform force and the moment resolution are different. When we consider acquisition environment noise at low frequencies, the force resolution is of the order of 10^{-4} N, and the resolution at frequencies above 200 Hz can reach the order of 10^{-5} N. The resolution of the platform moment is of the order of 10^{-6} Nm. If the signal can be identified by its SNR of 10, the force resolution should be at least 10^{-3} N and the moment is of the order of 10^{-4} Nm. Of course, these are theoretical

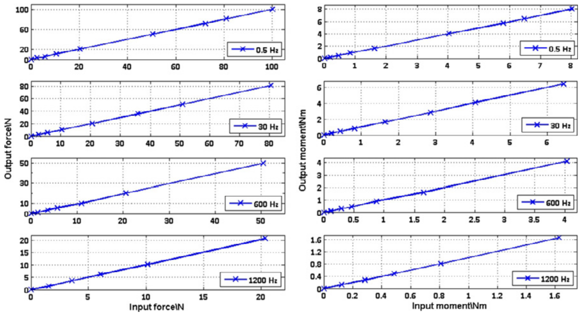

Fig. 18. Dynamic linearity test curves for the six-dimensional output.

Table 3
Average platform resolution in the 8–200 Hz range.

Frequency range	Resolution (N/Nm)					
	F_x	F_y	F_z	M_x	M_y	M_z
8–10 Hz	1.62×10^{-4}	1.75×10^{-4}	3.49×10^{-4}	1.16×10^{-5}	1.2×10^{-5}	7.1×10^{-6}
10–20 Hz	5.846×10^{-5}	3.73×10^{-5}	2.05×10^{-4}	3.74×10^{-6}	1.59×10^{-6}	2.9×10^{-6}
20–50 Hz	4.15×10^{-5}	1.72×10^{-5}	7.8×10^{-5}	4.45×10^{-6}	1.13×10^{-6}	3.38×10^{-6}
50–100 Hz	2.92×10^{-5}	1.89×10^{-5}	6.64×10^{-5}	5.22×10^{-6}	1.66×10^{-6}	4.94×10^{-6}
100–200 Hz	4.04×10^{-5}	1.03×10^{-5}	5.549×10^{-5}	8.54×10^{-6}	2.1×10^{-6}	5.18×10^{-6}

values, obtained without taking the real acquisition environment into account, so we can detect both the resolution and the precision via the following test.

Finally, we test the dynamic precision based on the relative error of the platform. A platform error analysis is then performed using the dynamic calibration matrix $\mathbf{W}(\omega)$ and the input impact signal from the hammer. The data acquisition device records the output voltage signals $\mathbf{V}(\omega)$ from the sensors, and we can then obtain the equivalent input excitation $\mathbf{F}(\omega)$ of the hammer using Eq. (4). The test results for the platform $\mathbf{F}_{ob}(\omega)$ are obtained through post-multiplication of the calibration matrix $\mathbf{W}(\omega)$ by the output voltage $\mathbf{V}(\omega)$; i.e.,

$$\mathbf{F}_{ob}(\omega) = \mathbf{W}(\omega)\mathbf{V}(\omega) \tag{23}$$

Therefore, the dynamic test errors of the six components can be obtained by comparing the equivalent input excitation with the test results. The relative error is calculated from:

$$\xi_i(\omega_j) = \frac{|\mathbf{F}_{obi}(\omega_j)| - |\mathbf{F}_i(\omega_j)|}{|\mathbf{F}_i(\omega_j)|} \times 100\%, \ \left(i = 1, 2 \cdots 6;\ j = 1, 2 \cdots n_{fft}\right) \tag{24}$$

where $\mathbf{F}_i(\omega_j)$ and $\mathbf{F}_{obi}(\omega_j)$ are both frequency domain complex matrices. To obtain the relative error, both $\mathbf{F}_i(\omega_j)$ and $\mathbf{F}_{obi}(\omega_j)$ use the magnitude of each element, where i represents the six components of the generalized force, and j is the element number of the matrix, which represents different frequencies. An error analysis of the six components of the disturbance force in each band allows comparison to be made between the actual values and the test results (see Fig. 19). From Fig. 19, we know that, based on consideration of a sufficient SNR (i.e., more than 10), the three force components of the test resolution can reach 0.001 N within the frequency range, and the three moment components of the test resolution can reach 0.0001 Nm. Table 4 and Table 5 present the maxima and the root mean square (RMS) values of the relative errors of the six components in the

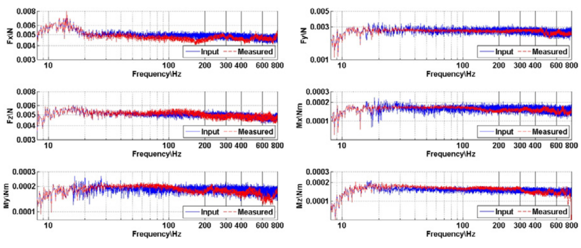

Fig. 19. Comparison of measured forces with input generalized forces.

Table 4
Dynamic relative measurement errors in the 8–800 Hz range.

Frequency range	Relative error (%)					
	F_x	F_y	F_z	M_x	M_y	M_z
8–50 Hz	1.57	1.61	1.25	1.17	1.43	4.23
50–100 Hz	4.62	0.89	2.56	1.32	2.33	3.73
100–150 Hz	6.66	1.43	4.98	0.88	1.55	4.72
150–200 Hz	7.04	3.87	1.77	1.50	4.44	3.46
200–250 Hz	4.56	3.28	2.93	1.93	5.21	3.82
250–300 Hz	0.35	0.31	3.32	1.54	2.68	4.22
300–350 Hz	1.65	1.55	1.47	3.86	3.77	5.21
350–400 Hz	5.08	0.76	1.41	2.49	4.89	6.89
400–450 Hz	4.421	3.01	2.22	3.21	4.21	3.38
450–500 Hz	4.59	1.89	2.49	4.55	4.64	6.54
500–550 Hz	2.39	3.54	0.27	0.85	4.66	2.11
550–600 Hz	0.52	2.84	0.60	2.32	3.76	3.21
600–650 Hz	0.24	2.37	0.84	3.89	5.18	5.01
650–700 Hz	1.12	1.84	4.10	4.90	4.27	4.71
700–750 Hz	3.34	4.421	0.35	5.11	5.33	4.62
750–800 Hz	3.53	4.126	3.47	5.57	7.75	13.45

Table 5
RMS values of the generalized force in dynamic measurements.

	F_x (N)	F_y (N)	F_z (N)	M_x (Nm)	M_y (Nm)	M_z (Nm)
RMS	4.0755e-4	3.8275e-4	3.84975e-4	3.8142e-5	2.5005e-5	4.5039e-5

8–800 Hz range. The dynamic relative error is mostly within 5% for all six components in the 8–800 Hz range and is required for micro-vibration testing of the large space telescope; the peak value (PV) is approximately 10%, and the RMS values of the relative errors are less than 4.1e−4 N and 4.5e−5 Nm. This test precision is at the same level as that of the light-load measurement systems that are commonly used in aerospace applications and can thus meet the requirements of micro-vibration measurements of vibration sources in large space telescopes.

4.3. Static mechanical performance test

Because a generalized-force measurement platform has been proposed, the static mechanical performance, which can be used to verify the reliability of the measurement data, should not be neglected in the performance test. To test the static mechanical characteristics of the platform, such as its linearity, repeatability, and inter-dimensional coupling, a static characteristic test system was also designed and built (Fig. 20). In addition, because of the attenuation of the piezoelectric signal, the peak before attenuation can be regarded as the output signal of the static force. Various standard forces and torques were applied at the geometric center of the platform using pulleys and weights. The real-time time data were processed using the previously-obtained dynamic calibration matrix $\mathbf{W}(\omega)$ and a fast Fourier transform (FFT). The range limits for the forces and moments in this test are 1 kN and 200 Nm, respectively.

In the static mechanical performance test, the force sensor (208C03, PCB; sensitivity: 2.248 mV/N; resolution: 0.02 N-rms; range: 2.224 kN) is used to monitor the loading force. Weights (5 kg; precision: ±1%) are loaded on the pulley one by one, where the pulley is connected to the platform using a rope. This loading and unloading cycle is performed three times. The

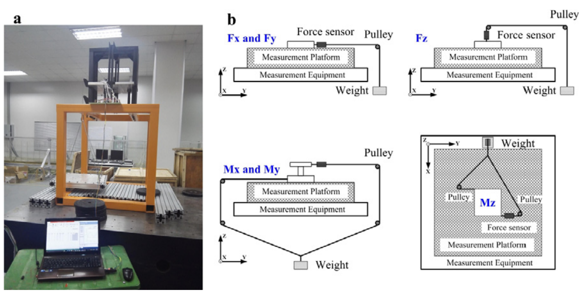

Fig. 20. Static mechanical performance test system. (a) Photograph of static mechanical performance test system, and (b) schematic illustration of static mechanical performance test system.

real-time data of the stable voltage (or the voltage peak) are recorded at every loading or unloading step (Fig. 21). Using the dynamic calibration matrix $\mathbf{W}(\omega)$ and the FFT, we then obtain the real-time six-dimensional frequency-domain data information. Table 6 shows the coupling interference of the platform determined from the static characteristic experimental data. The interference in the platform measurement data mainly comes from dimensional errors and assembly errors, and can also be corrected using the static calibration matrix. The other static characteristics of the platform that were processed using the static calibration matrix are listed in Table 7. The measurement platform linearity is within 0.1%FS. The repeatability is within 0.1%FS, and the static relative error of the platform is within 5%FS.

5. Conclusions

This article has described the analysis, design and testing of a novel dynamic disturbance measurement platform for large vibration sources. The platform uses redundant piezoelectric sensors to increase its stiffness and its measurement range, while the precision is improved through use of an efficient algorithm. The experimental results show that the first-order fundamental frequency is more than 1300 Hz, while the corresponding range is more than 40 kN. The dynamic relative error in the 8–800 Hz range is largely less than 5%, while the PV remains near 10%. The static relative error of the platform is within 5%. The linearity of the platform is within 0.1%FS, and the repeatability is within 0.1%FS. The research results show that the platform provides advances in terms of its high rigidity and its measurement range and precision. Further investigations of this measurement platform will focus on the rigid-flexible coupling theory of the vibration source and the measurement platform.

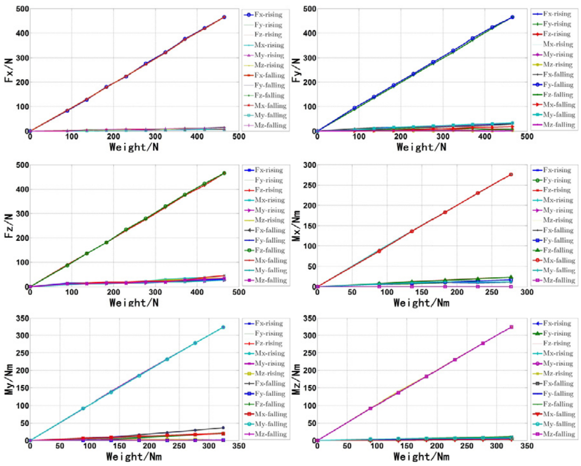

Fig. 21. Relationship curves between input load and output load.

Table 6
Coupling interference of sensors obtained experimentally.

Force/Moment (N; Nm)	Coupling interference (%)					
	F_x	F_y	F_z	M_x	M_y	M_z
F_x	–	3.9%	4.3%	1.7%	2.3%	2.9%
F_y	5.1%	–	6.7%	5.7%	8.1%	0.3%
F_z	5.5%	6.5%	–	8.8%	5.7%	5.3%
M_x	2.0%	6.0%	9.4%	–	4.2%	1.3%
M_y	6.4%	2.2%	9.2%	6.0%	–	2.3%
M_z	2.7%	0.4%	5.4%	1.0%	2.4%	–

Table 7
Statistics of static performance results.

Force/Moment (N; Nm)	Sensor sensitivity (N/N; Nm/Nm)	Nonlinearity (%FS)	Repeatability error (%FS)	Stability relative error (%FS)
F_x	1.07	0.08	0.08	2.02
F_y	1.08	0.09	0.03	3.61
F_z	1.08	0.09	0.02	2.43
M_x	1.03	0.08	0.06	1.15
M_y	1.02	0.03	0.08	0.71
M_z	1.02	0.01	0.07	0.82

Author contribution

Zhenbang Xu and Mingyi Xia contributed to the conception of the study; Mingyi Xia contributed significantly to analysis and manuscript preparation; Kang Han, Qi Huo and Ang Li contributed to the experiment design and operation; Mingyi Xia performed the data analyses and wrote the manuscript; Zhenbang Xu helped perform the analysis with constructive discussions.

Funding

This work was supported by the National Natural Science Foundation of China [grant number 11672290]; the Jilin Scientific and Technological Development Program [grant number 20160520074JH].

References

[1] D. Addari, G.S. Aglietti, M. Remedia, Experimental and numerical investigation of coupled microvibration dynamics for satellite reaction wheels, J. Sound Vib. 386 (2016) 225–241.
[2] F. Deng, X. He, J. Zhang, L. Li, X. Dong, Research on the effects of microgravity vibration environment in the spacelab, J. Vib. Shock 24 (3) (2005) 103–107.
[3] O.L. de Weck, D.W.M. Iller, H. Guiterrez, Structural dynamics and control for ngst - a preliminary study, in: Proceedings of the 34th Lige International Astrophysics Colloquium, Lige, 1998. Belgium.
[4] R. Masterson, D.W. Miller, R.L. Grogan, Development and validation of reaction wheel disturbance models: empirical model, J. Sound Vib. 249 (3) (2002) 575–598.
[5] Z. Zhang, G. Aglietti, Microvibration modelling and testing of a satellite reaction wheel, in: Proceedings of the European Conference of Mechanical Engineering (ECME'11), 2011. Puerto De La Cruz, Tenerife.
[6] P.Y. Bely, O.L. Lupie, J.L. Hershey, Line-of-sight jitter of the Hubble space telescope, in: Optical Engineering and Photonics in Aerospace Sensing, Int. Soc. Opt. Photonics, 1993, pp. 55–61.
[7] P.Y. Bely, in: The Design and Construction of Large Optical Telescopes, Springer-Verlag, New York, 2003.
[8] T.T. Hyde, K.Q. Ha, J.D. Johnston, J.M. Howard, G.E. Mosier, Integrated modeling activities for the James Webb space telescope: optical jitter analysis, in: Proceedings of the SPIE Conference on Astronomical Telescopes and Instrumentation, 2004. Glasgow, Scotland.
[9] A.J. Bronowicki, Vibration isolator for large space telescopes, J. Spacecr. Rocket. 43 (2006) 45–53.
[10] A.J. Bronowicki, J.W. Innis, A family of full spacecraft-to-payload isolators, Technol. Rev. J. Fall/Winter (2005) 21–41.
[11] V. Preda, J. Cieslak, D. Henry, et al., A H_∞/μ, solution for microvibration mitigation in satellites: a case study, J. Sound Vib. 399 (2017) 21–44.
[12] Y.J. Li, B.Y. Sun, J. Zhang, et al., A novel parallel piezoelectric six-axis heavy force/torque sensor, Measurement 42 (5) (2009) 730–736.
[13] Y. Sun, Y. Liu, T. Zou, et al., Design and optimization of a novel six-axis force/torque sensor for space robot, Measurement 65 (2015) 135–148.
[14] Q. Liang, D. Zhang, Q. Song, et al., Design and fabrication of a six-dimensional wrist force/torque sensor based on E-type membranes compared to cross beams, Measurement 43 (10) (2010) 1702–1719.
[15] J.W. Joo, K.S. Na, D.I. Kang, Design and evaluation of a six-component load cell, Measurement 32 (32) (2002) 125–133.
[16] L.P. Chao, K.T. Chen, Shape optimal design and force sensitivity evaluation of six-axis force sensors, Sens. Actuators, A 63 (2) (1997) 105–112.
[17] S.A. Liu, H.L. Tzo, A novel six-component force sensor of good measurement isotropy and sensitivities, Sens. Actuators, A 100 (2) (2002) 223–230.
[18] G.S. Kim, H.J. Shin, J. Yoon, Development of 6-axis force/moment sensor for a humanoid robot's intelligent foot, Sens. Actuators, A 141 (2) (2008) 276–281.
[19] Y. Lu, Y. Wang, N. Ye, et al., Development of a novel sensor for hybrid hand with three fingers and analysis of its measure performances, Mech. Syst. Signal Process. 83 (2016) 116–129.
[20] Z.Y. Jia, S. Lin, W. Liu, Measurement method of six-axis load sharing based on the Stewart platform, Measurement 43 (3) (2010) 329–335.
[21] Y. Hou, D. Zeng, J. Yao, et al., Optimal design of a hyperstatic Stewart platform-based force/torque sensor with genetic algorithms, Mechatronics 19 (2) (2009) 199–204.
[22] R. Ranganath, P.S. Nair, T.S. Mruthyunjaya, et al., A force–torque sensor based on a Stewart Platform in a near-singular configuration, Mech. Mach. Theor. 39 (9) (2004) 971–998.
[23] Ying-jun Li, Gui-cong Wang, Zhao Dong, Xuan Sun, Qing-hua Fang, Research on a novel parallel spoke piezoelectric 6-DOF heavy force/torque sensor, Mech. Syst. Signal Process. 36 (1) (2013) 152–167.
[24] R. Liang, Q.M. Wang, High sensitivity piezoelectric sensors using flexible PZT thick-film for shock tube pressure testing, Sens. Actuators, A 235 (2015) 317–327.
[25] D. Durand, C. France, Measurement Sensor for a Linking Wrench between Two Mechanical Parts, as Well as its Manufacturing Process, 1998. US, US005821431A[P/OL].
[26] Y. Sujan, G. Uma, M. Umapathy, Design and testing of piezoelectric resonant pressure sensor, Sens. Actuators, A 250 (2016) 177–186.
[27] J.P. Chen, C. Wei, M.Y. Xia, An ultra-low frequency micro-vibration testing platform based on strain-resistance effect, J. Vib. Shock 24 (33) (2014) 77–81.
[28] L. Ye, M. Yang, L. Xu, et al., Optimization of inductive angle sensor using response surface methodology and finite element method, Measurement 48 (1) (2014) 252–262.
[29] B. Wu, J. Luo, F. Shen, et al., Optimum design method of multi-axis force sensor integrated in humanoid robot foot system, Measurement 44 (9) (2011) 1651–1660.
[30] Q. Luo, L. Tong, Design and testing for shape control of piezoelectric structures using topology optimization, Eng. Struct. 97 (2015) 90–104.
[31] Y.J. Li, J. Zhang, Z.Y. Jia, et al., Research on force-sensing element's spatial arrangement of piezoelectric six-component force/torque sensor, Mech. Syst. Signal Process. 23 (8) (2009) 2687–2698.
[32] Y.J. Li, G.C. Wang, J. Zhang, et al., Dynamic characteristics of piezoelectric six-dimensional heavy force/moment sensor for large-load robotic manipulator, Measurement 45 (5) (2012) 1114–1125.
[33] N. Hu, H. Fukunaga, S. Matsumoto, et al., An efficient approach for identifying impact force using embedded piezoelectric sensors, Int. J. Impact Eng. 34 (7) (2007) 1258–1271.
[34] X.B. Chen, Z.J. Yuan, Y.X. Yao, Study on calibration of 6-axis wrist force sensors for robot, Robot 19 (1) (1997) 7–12.